# Source Reconstruction for IC Radiated Emissions Based on Magnitude-Only Near-Field Scanning

Ji Zhang and Jun Fan, *Fellow Member, IEEE*

***Abstract*—Near-field scanning with phase measurement is always a challenge in practical experiments because of its complexity and lack of accuracy. Therefore, utilizing the magnitude-only information to achieve phase-retrieval and emissions source reconstruction is preferred. This paper proposes a fast and accurate algorithm that can model the emissions from ICs by generating a set of equivalent dipole elements. The process of this algorithm only requires the information of the field magnitudes on two near-field scanning planes of different heights. Unlike other conventional source reconstruction techniques (such as genetic algorithm, gradient optimization), the proposed approach iteratively performs the back-and-forth transformations among the fields and equivalent dipole elements. By optimizing the locations of the equivalent dipole array and the initial values of these dipole elements, the iteration process is capable of quickly converging to the correct electromagnetic field values, including both magnitude and phase. The fields recovered from the calculated equivalent dipole sources have been validated by comparing to the fields emitted from a practical IC source.**

***Index Terms*—Equivalent dipole elements, IC emissions, iteration algorithm, phase retrieval, source reconstruction.**

## I. Introduction

AN ACCURATE prediction on the emission behavior of component-level electronic devices is always of great interest for designers and electromagnetic compatibility (EMC) engineers. Usually the information of physical sources is difficult to capture and simulate; thus, researchers try to utilize the scanned near-field on a plane above the device under test (DUT) to extract sufficient field information. There are multiple ways of estimating the emitting fields based on the near-field data. One of the ideas is to perform a direct fields-transformation from the scanned plane to another higher plane, or from the scanned plane to far-field [1]–[3]. This method is based on the plane-wave spectrum theory or integral equations. Another way of using the near-field data is to build up a set of equivalent dipoles at the DUT's location, by solving a set of linear equations [4]–[7]. However, most of these ways require capturing the near-field, including both magnitude and phase information, while the phase-resolved near-field measurement is always a challenge in practical tests.

Some groups developed practical techniques for phase measurement, but each one has its own unavoidable drawbacks. In [4] and [8], two techniques were described: one is to use a vector network analyzer (VNA) with external reference function; the other is to use a spectrum analyzer combined with a hybrid coupler. The expensive instrument such as the VNA is not affordable for every laboratory, besides the fact that the reference port often has a limited dynamic range. A spectrum analyzer is common for most of the laboratories, but the phase measurements need at least three times of sweeps under different hybrid settings. A time-domain scanning was introduced in [9]–[11]: after postprocessing the recorded time-domain waveform by fast Fourier transform (FFT), the phase-resolved field mapping can be provided. However, the low signal-to-noise ratio is always one of the disadvantages of time-domain measurements.

Because of the difficulties of phase-resolved near-field measurements, a source reconstruction method that only needs the magnitude information during the near-field scanning is preferred. In [12]–[14], two phase retrieval methods were mentioned: the adjoint field method and the phase angle gradient method (PAGM). Both methods used the scanned field amplitudes on three planes at different heights. In the adjoint field method, the equivalent dielectric between plane #1 and plane #2 was searched by a gradient-based algorithm; then, the properties of the equivalent dielectric combined with the sources on plane #1 were used to calculate the correct fields on other planes. For the PAGM, the unknown variables were the phase angles of the fields on plane #1. A gradient-based technique was employed to find the proper phase angles which can minimize the error between the measured and calculated field amplitudes on other planes. Another optimization based technique was proposed in [15]–[17] where the difference of the square amplitude was used as the basic terms of the cost function, rather than the difference of the amplitudes, and the unknown variables were the complex fields on the first plane, instead of the phase angles. The cost function allowed obtaining a quadratic operator which can reduce the local-minimal problems.

Some other groups tried to solve this optimization problem by employing the genetic algorithm (GA) rather than the gradient technique. As mentioned in [18] and [19], the strategy was to find a set of $N$ dipoles as the equivalent sources that generate the same field magnitudes on the scanning planes at

Manuscript received October 4, 2016; revised November 28, 2016; accepted December 9, 2016. Date of publication January 4, 2017; date of current version January 25, 2017. This work was supported by the National Science Foundation under Award no. IIP-1440110.

The authors are with the Electromagnetic Compatibility Laboratory, Missouri University of Science and Technology, Rolla, MO 65409, USA (e-mail: jz7r9@mst.edu; jfan@mst.edu).

Color versions of one or more of the figures in this paper are available online at http://ieeexplore.ieee.org.

Digital Object Identifier 10.1109/TEMC.2016.2638760

different heights. In GA, each individual consists of *N* dipoles, and each dipole consists of a few coded genes, representing the type (electric or magnetic) of dipole, the magnitude and phase value, the location, and the orientation. However, the number of the equivalent dipoles in GA is often strictly limited due to the complex searching procedure.

Another set of phase-retrieval techniques come from the antenna application area and electron microscopy area. The basic principle is to perform an iterative transformation of the fields back and forth between different scanning planes. This method was first proposed by Gerchberg and Saxton [20] for the problems of electron microscopy, and the transformation iteration was performed between the modulus data at the aperture plane and the modulus data at far-field. Later, the application of this method was extended from the optical problems to the image-reconstruction problem associated with the antenna diffraction, in [21]–[23]. The fields in the imaging region were the recovery object, and the iteration transformation was performed between the object plane and two other planes. Some examples were used to validate this algorithm, such as the recovered imaging field of a reflector antenna and the recreated aperture field of a slotted waveguide array.

In this work, the idea of back-and-forth iteration is further extended to the application of near-field source reconstruction. A set of equivalent dipole sources are reconstructed to represent an emitting integrated circuit. Unlike other optimization methods (such as GA), there is no limitation on the number of dipole moments. These dipole moments are uniformly spread at the location of the emitting IC. The magnitudes of the fields at two planes above the IC are first scanned; then, the iterative transformation keeps running among the dipole moments and the EM fields on the two scanning planes while the measured field magnitudes are used as the restriction condition during the iteration. Finally, the magnitude error between the calculated and measured fields is reduced to the accepted value with a certain tolerance.

The procedure of the iteration algorithm is introduced in Section II, and the transformation steps among dipole moments and fields are described in detail in Section III. Section IV briefly discusses how to determine the initial values for the equivalent dipole moments. Two validation cases are used to validate the proposed methodology in Section V, followed by the conclusions in Section VI.

## II. Iteration Algorithm Based on Magnitude of Near-Field Data

A set of uniformly spread dipole elements in an array are assigned at the location of an emitting IC as the equivalent sources. These equivalent dipoles will be calculated through the proposed algorithm to describe the real emission behavior of the IC. Considering the actual structure of the IC, the major physical radiation sources usually are the conductive current flowing along with the pins/bonding wires, and the vertical displacement current due to the time-varying voltage between frame-flag and return plane. Therefore, it is reasonable to use only three types of dipoles to represent the emission behavior

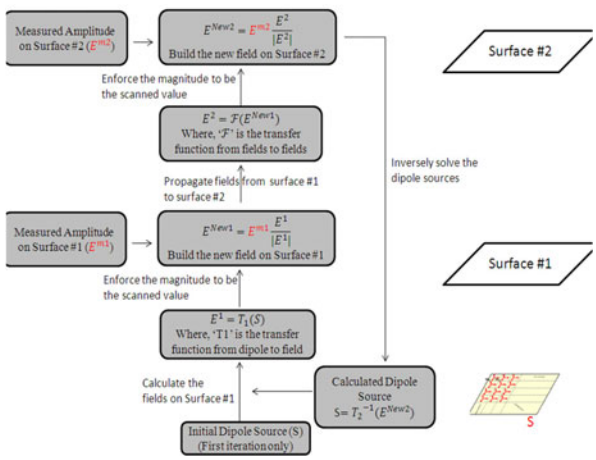


Fig. 1. Back-and-forth iteration algorithm for emission source reconstruction.

of the whole IC: the vertically orientated electrical dipole moments and horizontally orientated magnetic dipole moments (along the $\hat{x}$ and $\hat{y}$ directions). The number and the positions of these equivalent dipoles are fixed, while the unknown parameters are the magnitudes and phase angles of these dipole elements.

The magnitudes of the electromagnetic fields on the two planes above the dipole-elements are scanned, recorded, and then utilized to complete the iteration procedure.

As shown in Fig. 1, the iteration algorithm starts with a set of initial values for the dipole sources (the ways of determining initial values will be introduced later), and then follows several actions:

*Step 1:* calculate the fields on surface #1 based on the initial dipole elements. Here, the transformation function T_1 is used to describe the relationship between the dipole elements and the fields on the first scanning plane.

*Step 2:* replace the magnitudes of the calculated fields on surface #1 with the corresponding scanned ones ($E^{m1}$). By this way, a set of new artificial fields can be generated with the scanned magnitudes and the calculated phase angles.

*Step 3:* propagate the artificial fields on surface #1 to the second scanning plane (surface #2). In the flow chart, *F* is the transformation function between the fields on the two planes.

*Step 4:* similar to step 2, replace the magnitudes of the calculated fields on the second scanning plane with the corresponding scanned ones ($E^{m2}$) so that the new artificial fields on surface #2 are established.

*Step 5:* back transform the artificial fields on the second scanning plane to the equivalent dipoles. $T_2$ is the transformation function from dipoles to the fields on the second plane, while ${T_2}^{-1}$ is the inverse transformation function from the fields to the dipoles.

*Step 6:* repeat the procedure from Step 1, while using the back-transformed dipoles to replace the initial dipoles.

The iteration will continue by following the above-mentioned steps, until a convergence condition can be satisfied. Here, we define the convergence condition by a relative-error function

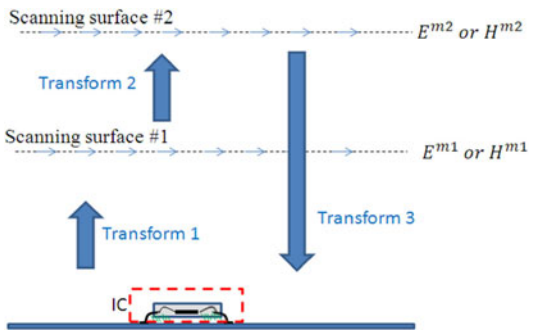


Fig. 2. Three critical transformations during iterations.

considering the EM fields on both the lower and higher planes:

$$\mathrm{RE}_{1\mathrm{st}} = \frac{1}{2}\left(\frac{\sqrt{\sum_{N1}\left(|E1_{\mathrm{scan}}|-|E1_{\mathrm{recover}}|\right)^2}}{\sqrt{\sum_{N1}\left(|E1_{\mathrm{scan}}|\right)^2}} + \frac{\sqrt{\sum_{N1}\left(|H1_{\mathrm{scan}}|-|H1_{\mathrm{recover}}|\right)^2}}{\sqrt{\sum_{N1}\left(|H1_{\mathrm{scan}}|\right)^2}}\right) \tag{1a}$$

$$\mathrm{RE}_{2\mathrm{nd}} = \frac{1}{2}\left(\frac{\sqrt{\sum_{N2}\left(|E2_{\mathrm{scan}}|-|E2_{\mathrm{recover}}|\right)^2}}{\sqrt{\sum_{N2}\left(|E2_{\mathrm{scan}}|\right)^2}} + \frac{\sqrt{\sum_{N2}\left(|H2_{\mathrm{scan}}|-|H2_{\mathrm{recover}}|\right)^2}}{\sqrt{\sum_{N2}\left(|H2_{\mathrm{scan}}|\right)^2}}\right) \tag{1b}$$

$$\mathrm{RE} = \frac{1}{2}\left(\mathrm{RE}_{1\mathrm{st}} + \mathrm{RE}_{2\mathrm{nd}}\right) \tag{1c}$$

where $\mathrm{RE}_{1\mathrm{st}}$ is the relative error of the field magnitudes on the lower plane, $\mathrm{RE}_{2\mathrm{nd}}$ is the relative error of the field magnitudes on the higher plane, $N1$ is the number of the scanning points on surface #1, $N2$ is the number of the scanning points on surface #2; $|E1_{\mathrm{scan}}|$ and $|H1_{\mathrm{scan}}|$ are the magnitudes of the scanned $E$ and $H$ fields at each point on surface #1, $|E2_{\mathrm{scan}}|$ and $|H2_{\mathrm{scan}}|$ are the magnitudes of the scanned $E$ or $H$ fields at each point on surface #2; $|E1_{\mathrm{recover}}|$ and $|H1_{\mathrm{recover}}|$ are the magnitudes of the calculated fields at each point on surface #1, $|E2_{\mathrm{recover}}|$ and $|H2_{\mathrm{recover}}|$ are the magnitudes of the calculated fields at each point on surface #2. As long as the relative error defined by (1) is reduced below a certain level (e.g., 5%), the iteration stops and the reconstructed dipoles at that moment are the final results.

## III. Transformation Functions During the Iterations

During the iteration, the transformation functions between dipoles and fields (or between fields and fields) are substantial for the whole source reconstruction procedure. As shown in Fig. 2, there are three critical transformations: transformation #1 is from the equivalent dipoles to the fields on the first scanning plane, transformation #2 is the field propagation from the first scanning plane to the second scanning plane, and transformation #3 is from the fields on the second plane back to the equivalent dipoles.

### A. Transformations Between Dipole-Elements and Fields

The relationship between the fields and the three types of dipole moments on an infinitely large perfect electrical conductor (PEC) plane is described in [7], and [24]–[26]. The fields at any scanning points can then be expressed as the superposition of the fields from all the equivalent dipole moments as a set of linear equations as

$$\begin{bmatrix}[E_x]_{M\times1}\\ [E_y]_{M\times1}\\ [H_x]_{M\times1}\\ [H_y]_{M\times1}\end{bmatrix} = \mathrm{T}_{4M\times3L}\begin{bmatrix}[P_z]_{L\times1}\\ [M_x]_{L\times1}\\ [M_y]_{L\times1}\end{bmatrix} \tag{2}$$

where $M$ is the number of the total scanning points, $L$ is the number of the source-array grids, and the matrix T contains the transformation coefficients.

Transformation #1 shown in Fig. 2 is directly implemented according to (2). In the real application, the T matrix is easily generated as long as the scanning points as well as the locations and the number of the equivalent dipole sources are fixed.

Transformation #3 is the inverse problem of transform #1, usually implemented by using the linear optimization technique, such as the least square method, as

$$\begin{bmatrix}[P_z]_{L\times1}\\ [M_x]_{L\times1}\\ [M_y]_{L\times1}\end{bmatrix} = \left(\left(\mathrm{T}_{4M\times3L}\right)^T\mathrm{T}_{4M\times3L}\right)^{-1} \times \left(T_{4M\times3L}\right)^T\begin{bmatrix}[E_x]_{M\times1}\\ [E_y]_{M\times1}\\ [H_x]_{M\times1}\\ [H_y]_{M\times1}\end{bmatrix}. \tag{3}$$

However, because of the unavoidable errors in measurements, the EM-fields are never perfectly accurate. Assuming there is an unknown error vector $\mathrm{e}_{\mathrm{mea}}$ associated with the measured fields, an error vector $\mathrm{e}_{\mathrm{dipole}}$ results in the solved dipole moments as

$$\begin{bmatrix}[P_z]_{L\times1}\\ [M_x]_{L\times1}\\ [M_y]_{L\times1}\end{bmatrix} + \mathrm{e}_{\mathrm{dipole}} = \mathrm{T}^{+}\left(\begin{bmatrix}[E_x]_{M\times1}\\ [E_y]_{M\times1}\\ [H_x]_{M\times1}\\ [H_y]_{M\times1}\end{bmatrix} + \mathrm{e}_{\mathrm{mea}}\right) \tag{4}$$

where $\mathrm{T}^{+}$ is used to represent the matrix operation of $\left(\left(\mathrm{T}_{4M\times3L}\right)^T\mathrm{T}_{4M\times3L}\right)^{-1}\left(\mathrm{T}_{4M\times3L}\right)^T$.

The condition number of $\mathrm{T}_{4M\times3L}$, denoted as $k(\mathrm{T})$, is well known as the ratio of the largest and the smallest singular values of $\mathrm{T}_{4M\times3L}$. It can be proven that the solution error $\mathrm{e}_{\mathrm{dipole}}$ is

limited by this condition number:

$$\frac{\|\mathrm{e}_{\mathrm{dipole}}\|}{\left\|\begin{bmatrix}[P_z]_{L\times 1}\\ [M_x]_{L\times 1}\\ [M_y]_{L\times 1}\end{bmatrix}\right\|} \le k\,(\mathrm{T})\,\frac{\|\mathrm{e}_{\mathrm{mea}}\|}{\left\|\begin{bmatrix}[E_x]_{M\times 1}\\ [E_y]_{M\times 1}\\ [H_x]_{M\times 1}\\ [H_y]_{M\times 1}\end{bmatrix}\right\|}. \tag{5}$$

From (5), it is obvious that an ill-conditioned transformation matrix $\mathrm{T}_{4M\times 3L}$, which has a large condition number $k(\mathrm{T})$, can amplify the measurement errors in solving the inverse problem. On the other hand, a smaller condition number can lower the upper-bound of the solution error. Thus, ideally, a transformation matrix $\mathrm{T}_{4M\times 3L}$ with a small condition number should be constructed for the inverse problem.

There are several factors that can impact the condition number of the transformation matrix:

1) the total numbers of the scanning points and the dipole moments;
2) the internal difference of the EM-field values among the different rows of the field vector;
3) the locations of the scanning points and the dipole moments.

In order to represent all the radiating current elements along the pins and in the die of the IC, it is better to choose an equivalent dipole array with high grid density and large size. However, a large amount of the dipole moments certainly can result in a large condition number in the transformation matrix [i.e., $\mathrm{T}_{4M\times 3L}$ in (2)], adversely affecting the accuracy of the least square solution of the inverse problem. So, the total number of the equivalent dipole sources should be neither too large nor too small. The value needs to be adjusted and optimized based on the condition number. Fig. 3 is an illustration case regarding the impact on condition number: two scanning planes are at 5 and 9 mm heights, with the size of 100 mm × 100 mm, and the grid-resolution of 1 mm; the equivalent dipole moments array is located at 0.38 mm above the return plane. As shown in Fig. 3, with the increase of the dipole array size, the condition number rises quickly

For usual cases in which the strength levels of the *E* and *H* fields are quite different, a normalization technique needs to be used to reduce the condition number of the transformation matrix. Each row of the matrix $\mathrm{T}_{4M\times 3L}$ is divided by the maximum magnitude of the corresponding field component. The normalized expression of (2) is shown here: (eq.6) shown at the bottom of this page.

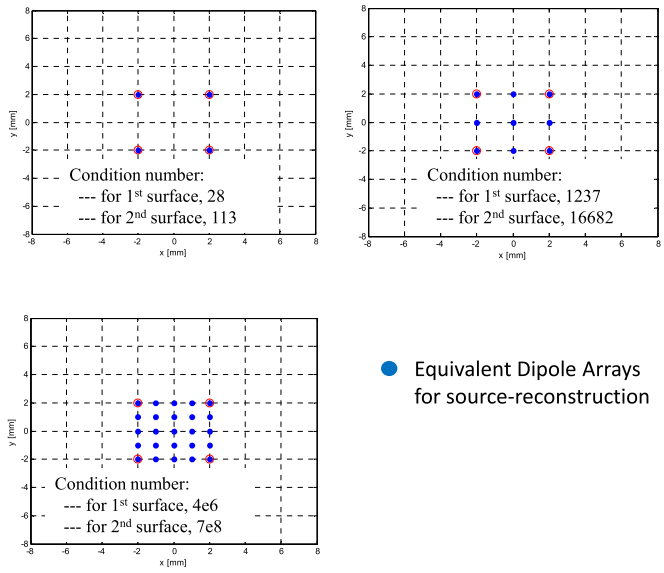


Fig. 3. Condition numbers of transformation matrices varying with dipole-arrays' sizes.

In this way, the effect of the difference between the magnitude levels of the *E* and *H* fields on the condition of the transformation matrix is minimized.

### B. Transformation Between Fields on Two Different Planes

Transformation #2 is to propagate the fields from the lower plane to the higher plane. In this work, it is based on the plane wave spectrum theory. From [27] to [29], in a source-free region, the Helmholtz equations for the electrical and magnetic fields can be derived as

$$\nabla^2\vec{\mathrm{E}} + {k_0}^2\vec{\mathrm{E}} = 0,\ \text{where } {k_0}^2 = \omega^2\varepsilon\mu, \tag{7}$$

$$\nabla^2\vec{\mathrm{H}} + {k_0}^2\vec{\mathrm{H}} = 0,\ \text{where } {k_0}^2 = \omega^2\varepsilon\mu. \tag{8}$$

One of the general solutions for these wave equations can be expressed in a plane wave form as

$$\vec{\mathrm{E}}\,(x,y,z) = \vec{T_E}\,(k_x,k_y)\,e^{-j(k_x x+k_y y+\gamma z)},\quad \text{where } {k_x}^2+{k_y}^2+\gamma^2 = {k_0}^2; \tag{9}$$

$$\vec{\mathrm{H}}\,(x,y,z) = \vec{T_E}\,(k_x,k_y)\,e^{-j(k_x x+k_y y+\gamma z)},\quad \text{where } {k_x}^2+{k_y}^2+\gamma^2 = {k_0}^2. \tag{10}$$

Once the frequency is fixed, there are only two independent variables among the three wave coefficients, because the square sum of $k_x$, $k_y$, and $\gamma$ is a constant value ${k_0}^2$. Any fields in the

$$\begin{bmatrix}[E_x]/max\{|E_x|\}\\ [E_y]/max\{|E_y|\}\\ [H_x]/max\{|H_x|\}\\ [H_y]/max\{|H_y|\}\end{bmatrix} = \begin{bmatrix}T_{E_x P_z}/\max\{|E_x|\} & T_{E_x M_x}/\max\{|E_x|\} & T_{E_x M_y}/\max\{|E_x|\}\\ T_{E_y P_z}/\max\{|E_y|\} & T_{E_y M_x}/\max\{|E_y|\} & T_{E_y M_y}/\max\{|E_y|\}\\ T_{H_x P_z}/\max\{|H_x|\} & T_{H_x M_x}/\max\{|H_x|\} & T_{H_x M_y}/\max\{|H_x|\}\\ T_{H_y P_z}/\max\{|H_y|\} & T_{H_y M_x}/\max\{|H_y|\} & T_{H_y M_y}/\max\{|H_y|\}\end{bmatrix}\begin{bmatrix}P_Z\\ M_x\\ M_y\end{bmatrix} \tag{6}$$

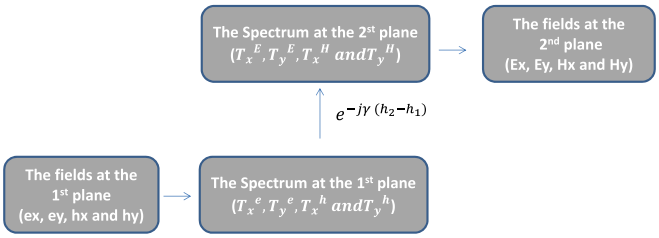


Fig. 4. Process of field transformation from lower plane to higher plane.

source-free region can then be expressed as the superposition of plane-waves with different amplitudes/phases associated with different pairs of $k_x$ and $k_y$ as

$$\vec{\mathrm{E}}(x,y,z) = \frac{1}{4\pi^2}\int_{-\infty}^{+\infty}\int_{-\infty}^{+\infty}\left[\vec{\mathrm{T}}_E(k_x,k_y) \times e^{-j\gamma z}\right] e^{-j(k_x x+k_y y)}dk_x dk_y, \quad (11)$$

$$\vec{\mathrm{H}}(x,y,z) = \frac{1}{4\pi^2}\int_{-\infty}^{+\infty}\int_{-\infty}^{+\infty}\left[\vec{\mathrm{T}}_H(k_x,k_y) \times e^{-j\gamma z}\right] e^{-j(k_x x+k_y y)}dk_x dk_y. \quad (12)$$

Actually, the integral expressions in (11) and (12) are in exactly the same mathematical form as a two-dimensional (2-D) inverse Fourier transform, and it can be implemented by 2-D inverse FFT. So the fields on a plane are projected onto a wave-coefficient domain, which is also called the "spectral domain." In order to calculate each term in the spectral domain, the 2-D Fourier transform can be used as

$$\vec{\mathrm{T}}_E(k_x,k_y)\,e^{-j\gamma z} = \int_{-\infty}^{+\infty}\int_{-\infty}^{+\infty}\vec{\mathrm{E}}(x,y,z)\,e^{j(k_x x+k_y y)}dxdy, \quad (13)$$

$$\vec{\mathrm{T}}_H(k_x,k_y)\,e^{-j\gamma z} = \int_{-\infty}^{+\infty}\int_{-\infty}^{+\infty}\vec{\mathrm{H}}(x,y,z)\,e^{j(k_x x+k_y y)}dxdy. \quad (14)$$

Obviously, the relationship between the spectral-domain terms at the lower plane and the corresponding ones at the higher plane is just a simple factor of $e^{-j\gamma h}$, where $h$ is the $z$-directional distance between the two planes. Without loss of generality, let us assume the $z$-coordinate of the lower plane is zero, and the higher plane is $h$. Furthermore, $\vec{\mathrm{T}}_E$ and $\vec{\mathrm{T}}_H$ are used to represent the spectral-domain terms $\vec{\mathrm{T}}_E(k_x,k_y)\,e^{-j\gamma z}$ and $\vec{\mathrm{T}}_H(k_x,k_y)\,e^{-j\gamma z}$. Then, we have

$$\vec{T}_E|_{z=h} = e^{-j\gamma h}\cdot\vec{T}_E(k_x,k_y) = e^{-j\gamma h}\cdot\vec{T}_E|_{z=0}, \quad (15)$$

$$\vec{T}_H|_{z=h} = e^{-j\gamma h}\cdot\vec{T}_H(k_x,k_y) = e^{-j\gamma h}\cdot\vec{T}_H|_{z=0}. \quad (16)$$

Now, the process of the field transformation from a lower plane to a higher plane becomes straightforward as shown in Fig. 4 as

1) obtain the tangential field components $E_x$ and $E_y$ (or $H_x$ and $H_y$) on the lower plane ($z = h1$);
2) follow (13) and (14) to obtain the spectral-domain terms of the $E$ and $H$ fields $\vec{\mathrm{T}}_E|_{z=h1}$ and $\vec{\mathrm{T}}_H|_{z=h1}$;


Fig. 5. Simple emitting-dipoles and the two observation planes.

3) calculate the spectral-domain terms at the higher plane ($z = h2$)

$$\vec{\mathrm{T}}_E|_{z=h2} = e^{-j\gamma(h2-h1)}\cdot\vec{\mathrm{T}}_E|_{z=h1};$$

$$\vec{\mathrm{T}}_H|_{z=h2} = e^{-j\gamma(h2-h1)}\cdot\vec{\mathrm{T}}_H|_{z=h1};$$

4) follow (11) and (12) to convert the spectral-domain terms on the higher plane to the EM fields ($E_x$, $E_y$ or $H_x$, $H_y$) on the higher plane.

Usually in the near-field region, the spectral-domain terms of electromagnetic fields consist of two different portions: the propagation wave and the evanescent wave. If ${k_x}^2 + {k_y}^2 < {k_0}^2$, the wave number along the $\hat{z}$ direction ($\gamma$) is a real number; thus, the $e^{-j\gamma z}$ term indicates a propagation wave along the $\hat{z}$ direction. When ${k_x}^2 + {k_y}^2 > {k_0}^2$, the wave number along the $\hat{z}$ direction ($\gamma$) becomes an imaginary number, and the $e^{-j\gamma z}$ term indicates a decaying wave. In the far-field region, most of the energy is concentrated within the circle of ${k_x}^2 + {k_y}^2 = {k_0}^2$ in the spectral domain, which means most of the wave components are propagating waves.

An example of the field transformation is given in Fig. 5. Two observation planes above the dipole sources are selected as 3 and 6 mm height. The frequency is set to be 5 GHz. The sampling resolution at each scanning plane is 1 mm, while the scanning region is 80 mm × 80 mm.

The field transformation as described in Fig. 4 is performed to calculate the fields on the higher plane according to the information on the lower plane. According to the 2-D FFT, the spatial-domain resolution of the sampled fields ($\Delta x$, $\Delta y$) and the spectral-domain resolution ($\Delta k_x, \Delta k_y$) have relationships given by

$$\begin{cases}\Delta k_x = \frac{2\pi}{\Delta x\cdot N}\\ \Delta k_y = \frac{2\pi}{\Delta y\cdot N}\end{cases} \quad (17)$$

when assuming the scanning region is a square shape consisting of $N \times N$ sampling points. The spatial-domain resolution of the sampled fields ($\Delta x$, $\Delta y$) and the maximum available wave-coefficients ($k_{x,\max}$, $k_{y,\max}$) have the relationships given by

$$\begin{cases}k_{x,\max} = \frac{\pi}{\Delta x\cdot N}(N-1) \approx \frac{\pi}{\Delta x}\\ k_{y,\max} = \frac{\pi}{\Delta y\cdot N}(N-1) \approx \frac{\pi}{\Delta y}\end{cases}. \quad (18)$$

In this example, the 80 mm × 80 mm scanning plane results in a very coarse spectral-domain resolution of 78 $\mathrm{m}^{-1}$, which is not fine enough compared with the value of $k_0$ (i.e., 104.8 $\mathrm{m}^{-1}$). Thus, 2-D zero-padding (which extends the scanning area to 300 mm × 300 mm) is applied to artificially improve the spectral-domain resolution.

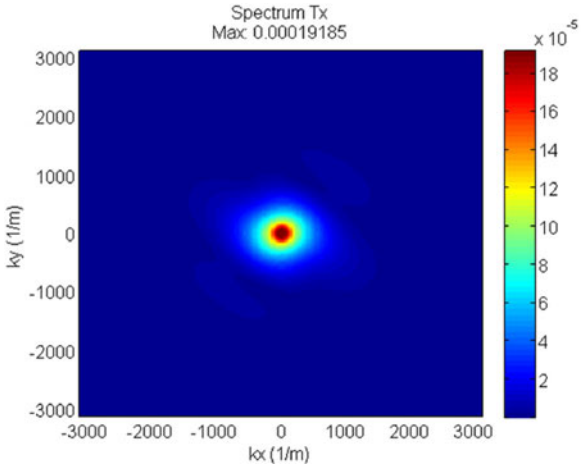


Fig. 6. Spectral-domain terms of $E_x$ field-component on the lower plane.

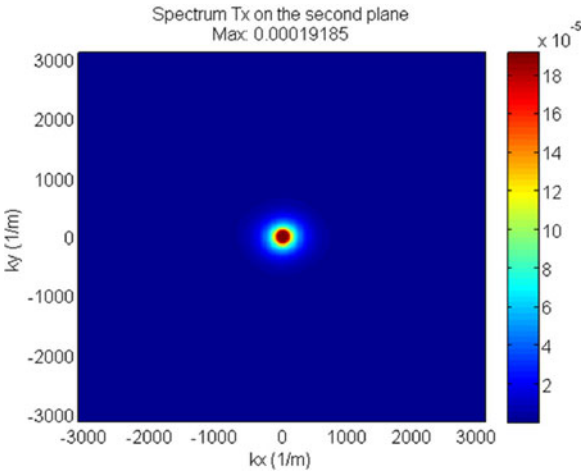


Fig. 7. Spectral terms of $E_x$ field-component on the higher plane.

Taking one of the field components $E_x$ as an example, the spectral-domain terms of $E_x$ on the lower plane (after zero-padding) is shown in Fig. 6. The transformation factor $e^{-j\gamma(h2-h1)}$ is then multiplied on each spectral-domain term. Within the circle of ${k_x}^2 + {k_y}^2 = {k_0}^2$, this transformation factor is just a phase shifting, as $\gamma$ is a real number; outside the circle of ${k_x}^2 + {k_y}^2 = {k_0}^2$, this transformation factor is an exponential attenuation on magnitude. Thus, the transformation of the spectral-domain terms from the lower plane to the higher plane works as a 2-D low-pass filter, whose flat-band is within the circle of ${k_x}^2 + {k_y}^2 = {k_0}^2$. The low-pass effect can be clearly observed by comparing the spectral-domain terms on the lower plane (shown in Fig. 5) with those on the higher plane (shown in Fig. 7).

The fields on the higher plane finally are calculated by performing the inverse 2-D FFT operation on the spectral-domain terms at the higher plane, following (11) and (12).

By using this plane-wave expansion method, the field transformation from the lower plane to the higher plane is achieved, demonstrated by comparing the original emitting fields on the higher plane in Fig. 8 with the transformed fields on the higher plane in Fig. 9.

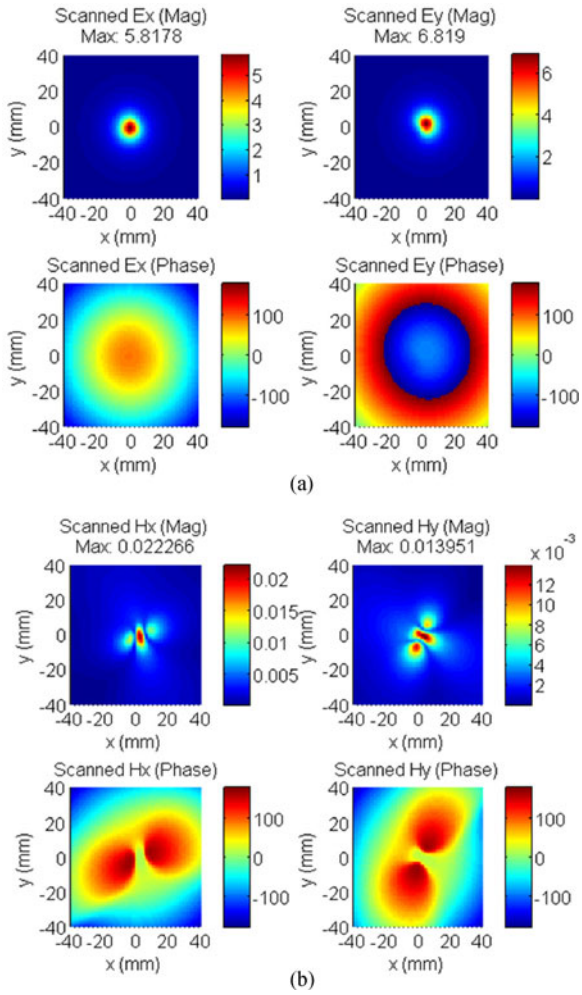


Fig. 8. Original emitted EM fields on the higher plane ($z = 6$ mm) ($E$ fields in unit of V/m and degree; $H$ fields in unit of A/m and degree).

## IV. Effectiveness and Accuracy of the Algorithm

### A. Initial Value

Initial value is always important for any kind of optimization technique, and this is especially true in this proposed iteration algorithm. A good initial value which is close to the global minimum points can significantly accelerate the convergence rate; on the other hand, some initial value could make the whole iteration algorithm trapped into a local minimum value. In this work, there are several options in determining the initial values for the equivalent dipole-sources.

The first method is to assign all of the dipole elements with the same magnitude and the same phase, and the rough magnitude level can be adjusted according to the measured radiation level.

In the second method, all the dipole elements can be assigned with the same magnitude but random phase distribution. The rough magnitude level can be adjusted according to the measured radiation level.

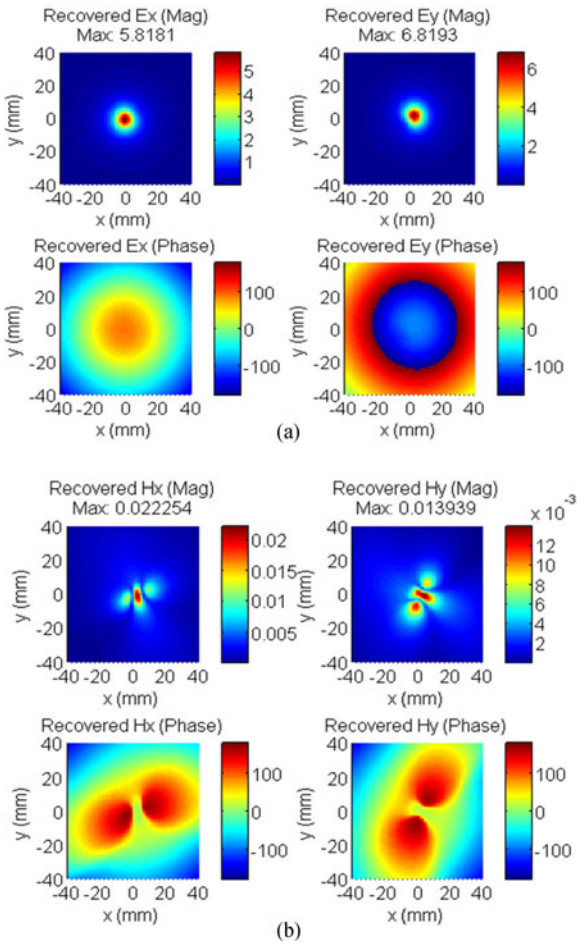


Fig. 9. Transformed EM fields on the higher plane ($z = 6$ mm) from the known EM fields on the lower plane ($E$ fields in unit of V/m and degree; $H$ fields in unit of A/m and degree).

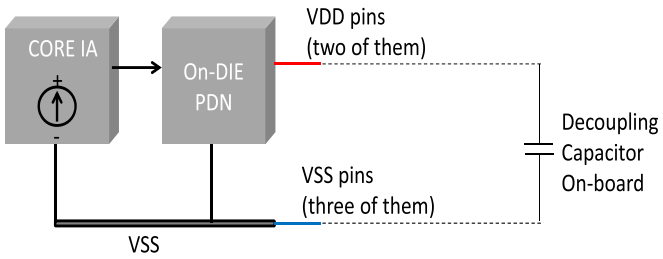


Fig. 10. Illustration of the ICEM architecture of a commercial IC.

The third method uses the known magnitude of the fields on the lower plane to reversely solve the initial dipoles based on the least square solution, by assuming that the field at every scanning point has the same phase. This could be a reasonable method for a relatively high scanning plane.

Finally, the fourth method is to use the known magnitudes of the fields on the higher plane to reversely solve the initial dipoles based on the least square solution, by assuming that the field at every scanning point has the same phase.

It is difficult to say which method is better, without looking at the real measured fields. Different ways of getting the initial values for the equivalent dipoles can be tried until a proper convergence of the iteration algorithm is observed.

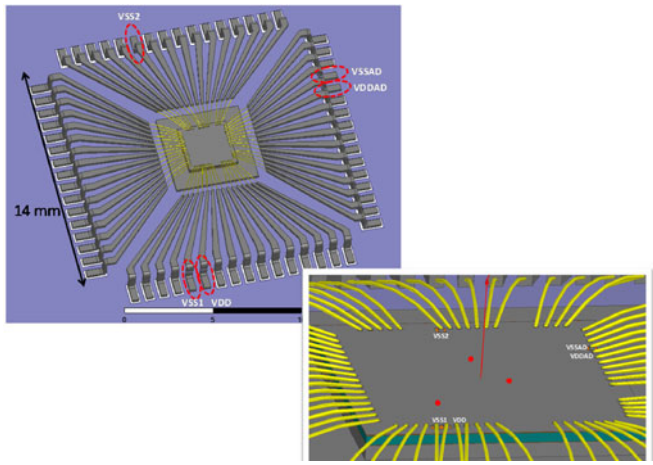


Fig. 11. PDN pins and bonding-wires within the package structure.

### B. Accuracy of Near-Field Measurements

The proposed reconstruction method is based on the magnitudes of the measured $E$ and $H$ fields on two surfaces; any measurement inaccuracy may result in reconstruction errors. We should reduce the near-field scanning error through several efforts. First of all, a careful calibration is needed in order to build a precise relationship between the $E/H$ fields at the field-probe tip and the output voltage of the field probe. Second, since our work does not require phase-scanning, the magnitudes of the fields can be measured with a spectrum analyzer. The resolution bandwidth of the spectrum analyzer should be narrow enough to maintain a low noise floor. Third, the tip of the field probe shall be as small as possible, which brings at least two benefits: the space resolution of probing points is improved, and the disruption of the probe body to the local fields is minimized.

## V. Validations of the Iterative Source-Reconstruction Algorithm

As mentioned at the very beginning, the final purpose of this work is to construct a set of equivalent dipole sources which can generate the same EM fields as from the real emitting IC. To demonstrate the proposed algorithm, an 8-Bit microcontroller (that is mainly applied in washing machines) was selected as the verification example. The IC has a 64-pin quad flat package. There are two power pins and three return pins in total, with 54 general purpose input/output (I/O) pins. In this verification example, a full-wave EM solver [Ansys high frequency structural simulator (a tool from Ansys Inc.) (HFSS)] (HFSS)) [25] was used to simulate the behavior of the IC emissions due to its internal activity source (IA) within the power delivery network (PDN). Then the magnitude information of the simulated fields on two different planes was used to achieve phase retrieval and source-reconstruction using the proposed iteration algorithm. Finally, the recovered near-field results were compared with the direct simulation results from the full-wave EM solver (reference data) to validate this iteration algorithm.

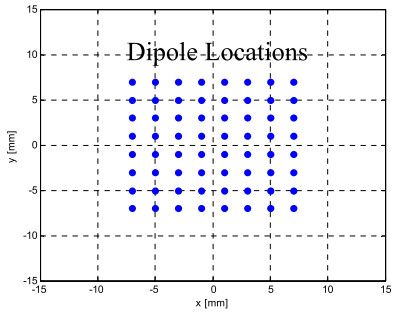


Fig. 12. Locations of the equivalent dipoles for IC emissions.

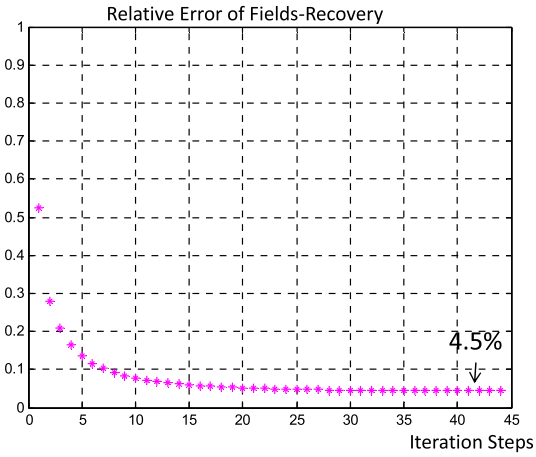


Fig. 13. Relative error during iteration (real IC as source, 500 MHz).

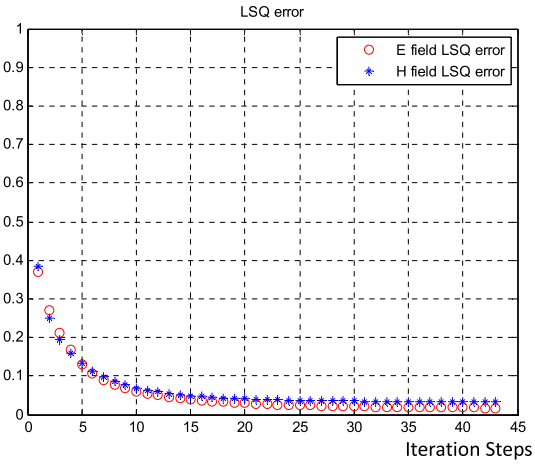


Fig. 14. Least-square-solution error during iteration (real IC as source, 500bMHz).

In a typical integrated circuit emission model (ICEM) modeling, the IA currents of the digital-core PDN are the major emitting sources, as shown in Fig. 10. Thus, during the full-wave simulations, a current source of 500 MHz was placed between the solid power/ground planes within the silicon substrate model. The current source fed currents into the power/ground planes and drove two power pins (VDD, VDDAD) and three return pins (VSS1, VSS2, and VSSAD).

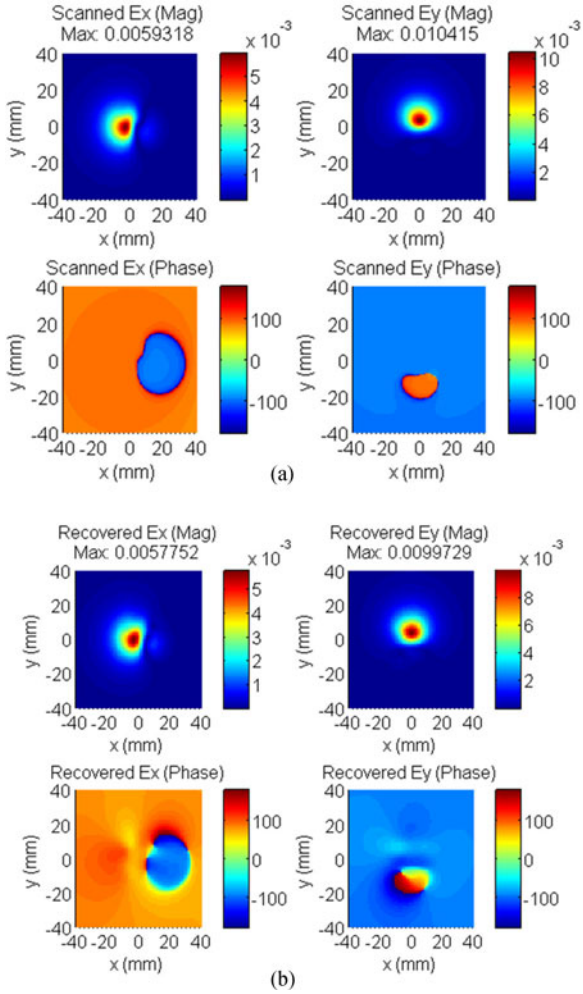


Fig. 15. Original and recovered $E$ fields at 9 mm (real IC as source, 500 MHz) ($E$ fields in unit of V/m and degree; $H$ fields in unit of A/m and degree).

In Fig. 11, the three-dimensional HFSS model of the IC, including the lead-frame package and the on-die PDN, is with a total size of $14 \times 14$ mm$^2$. Five PDN pins of the IC (two power pins and three return pins) are interconnected to the on-die PDN structure. Because there are usually large decoupling capacitors in the PDN of the circuit board, the power/return pins in our modeling were externally connected to one piece of PEC ground plane to represent the low power impedance of the board. All other IO pins besides the five PDN pins were also present in the model, but there were no IA sources stimulating them. The size of the on-die PDN is relatively small, and the edge length is no larger than 5 mm (see the zoomed-in plot at the lower-right corner of Fig. 11). In industrial design, the power and ground nets on silicon are often formed by metallic mesh-grid with high density or even solid planes. Here, two solid planes were used to represent the on-die power/ground nets; the thickness and the permittivity of the dielectric layer between the two planes were selected so that the power-ground capacitance was close to the actual on-chip power capacitance value (i.e., 1 nF). There was also a thin layer of $SiO_2$ beneath the silicon substrate to isolate the substrate from the metallic lead-frame-flag, with a capacitance of approximately 112 pF.

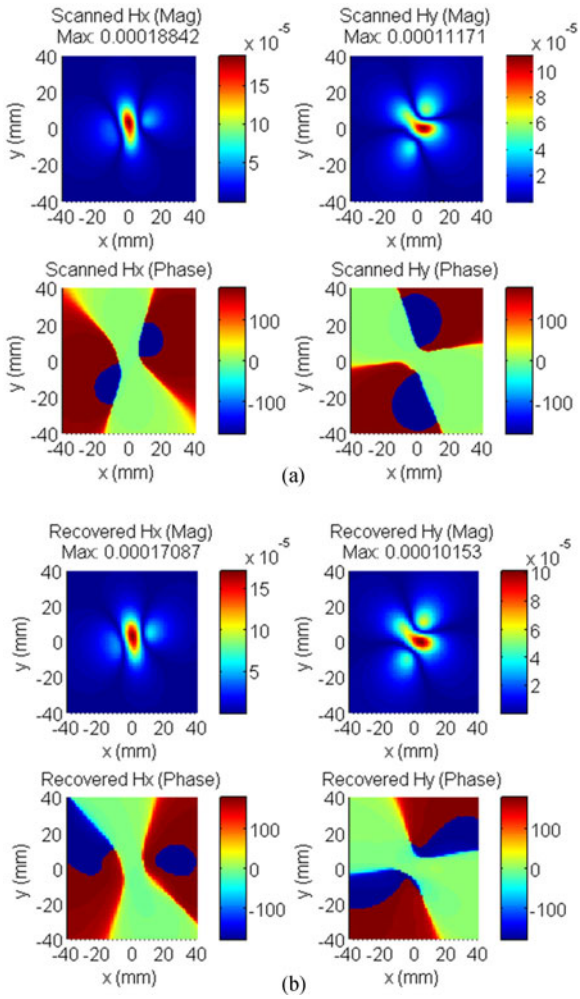


Fig. 16. Original and recovered $H$ fields at 9 mm (real IC as source, 500 MHz) ($E$ fields in unit of V/m and degree; $H$ fields in unit of A/m and degree).

In HFSS, the solution frequency was made the same as the frequency of the internal current source at 500 MHz. In order to ensure the computation accuracy, adaptively refined meshing was applied inside the computational domain. Furthermore, the mesh length on the two observation surfaces were manually enforced as 1 mm, which was significantly less than the wave length of 500 MHz in the free space. The size of the ground plane was 200 mm $\times$ 200 mm, which was large enough to be treated as an infinitely-large ground if compared with the dimensions of the IC.

The generated EM fields from this microcontroller were simulated and recorded on the two planes at 9 mm height and 12 mm height. The "scanning" plane size was 80 mm $\times$ 80 mm with a 1 mm spacing between neighboring "scanning" points. For the purpose of source reconstruction, the equivalent dipole sources were distributed in a uniformly spread array, with a size of 14 mm $\times$ 14 mm (which was the same as the IC package size) and a distance of 2 mm between neighboring dipole locations, as shown in Fig. 12.

Following the iteration process (shown in Fig. 1), the fast convergence can be observed in Fig. 13. After 30 steps, the iteration already approached to a steady and optimized result.

As the least square solution accuracy always plays an important role during the whole iteration algorithm, the least-squares (LSQ) errors, defined by root-mean-square deviation between the fields transformed during transformation #2 and the fields calculated with least-square solved dipoles by applying Eqs. (2), were recorded in every step and then plotted in Fig. 14. It can be seen that the LSQ error also keeps going down to a very small value, for both the $E$ and $H$ fields. The more intuitive comparisons between the original and recovered fields can be observed from the field patterns shown in Figs. 15 and 16. The success of phase retrieval on the $E$ and $H$ fields at both planes can clearly be seen.

## VI. Conclusion

In order to construct a set of equivalent sources that can represent the emission behavior of an emitting IC, the scanned near-fields above the IC are needed, usually requiring both magnitude and phase information. However, considering the difficulties of measuring phase, an iteration algorithm that is capable of achieving source reconstruction and phase retrieval from magnitude-only information of the near-fields is proposed in this paper. The magnitudes of the fields on two planes at different heights are recorded, and then used to constrain the amplitudes of the calculated fields during iterations. Three transformations (from equivalent dipoles to fields on the lower plane, from fields on the lower plane to the fields on the higher plane, and from fields on the higher plane back to the equivalent dipoles) are continued at each iteration step, until the convergence condition is achieved. This algorithm has been verified by using a set of dipole arrays to simulate the emission behavior of a commercial microcontroller.

## References

[1] A. Taaghol and T. K. Sarkar, "Near-field to near/far-field transformation for arbitrary near-field geometry utilizing an equivalent magnetic current," *IEEE Trans. Electromagn. Compat.*, vol. 38, no. 3, pp. 536–542, Aug. 1996.

[2] T. K. Sarkar and A. Taaghol, "Near-field to near/far field transformation for arbitrary near-field geometry utilizing an equivalent electric current and MoM," *IEEE Trans. Electromagn. Compat.*, vol. 47, no. 3, pp. 566–573, Mar. 1999.

[3] P. Petre and T. K. Sarkar, "Differences between modal expansion and integral equation methods for planar near-field to far-field transformation," *J. Electromagn. Wave Appl.*, vol. 10, no. 2, pp. 269–271, 1996.

[4] Y. Vives-Gilabert, C. Arcambal, A. Louis, F. De Daran, P. Eudeline, and B. Mazari, "Modeling magnetic radiations of electronic circuits using near-field scanning method," *IEEE Trans. Electromagn. Compat.*, vol. 49, no. 2, pp. 391–400, May 2007.

[5] P. F. Lopez, C. Arcambal, D. Baudry, S. Verdeyme, and B. Mazari, "Simple electromagnetic modeling procedure: from near-field measurements to commercial electromagnetic simulation tool," *IEEE Trans. Instrum. Meas.*, vol. 59, no. 12, pp. 3111–3121, Dec. 2010.

[6] A. Ramanujan, Z. Riah, A. Louis, and B. Mazari, "On the radiated electromagnetic emission modelling of on-chip microwave components," in *Proc. IEEE Int. Symp. Electromagn. Compat.*, Jul. 2010, pp. 647–651.

[7] Z. Yu and J. Fan, "An improved dipole-moment model based on near-field scanning for characterizing near-field coupling and far-field radiation from an IC," *IEEE Trans. Electromagn. Compat.*, vol. 55, no. 1, pp. 97–108, Feb. 2013.

[8] X. Tong, "Simplified equivalent modelling of electromagnetic emissions from printed circuit boards," Ph.D. dissertation, Univ. Nottingham, Nottingham, U.K., May 2010.

[9] T. Mager, C. Reinhold, C. Hedayat, and T. Gessner, "Near field scanner in time and frequency domain," *MST News*, vol. 1, pp. 40–41, 2009.
[10] T. Ordas, M. Lisart, E. Sicard, P. Maurine, and L. Torres, "Near-field mapping system to scan in time domain the magnetic emissions of integrated circuits," in *Proc. Int. Workshop Power Timing Model. Optim. Simul.*, 2008, pp. 229–236.
[11] T. Stadtler, L. Eiflter, and J. L. Ter Haseborg, "Double probe near field scanner, a new device for measurements in time domain," in *Proc. 2003 IEEE Int. Symp. Electromagn. Compat.*, vol. 18–22, Aug. 2003, pp. 86–90.
[12] M. Johansson, A. Fhager, H.-S. Lui, and M. Persson, "Comparison between two phase-retrieval methods for electromagnetic source modeling," *Prog. Electromagn. Res. B*, vol. 30, pp. 239–253, 2011.
[13] M. Johansson, L. E. Nord, R. Kopecky, A. Fhager, and M. Persson, "Computational methods for modeling of complex sources ,"*Int. J. Comput. Math. Electr. Electron. Eng.*, vol. 27, no. 1, pp. 133–143, 2008.
[14] M. Johansson, H.-S. Lui, and M. Persson, "Performance evaluation of phase-angle gradient method for phase retrieval based on low-frequency amplitude-only near-field data," *Prog. Electromagn. Res. B*, vol. 25, pp. 113–130, 2010.
[15] T. Isernia, G. Leone, and R. Pierri, "Radiation pattern evaluation from near-field intensities on planes," *IEEE Trans. Antennas Propag.*, vol. 44, no. 5, pp. 701–710, May 1996.
[16] T. Isernia, G. Leone, and R. Pierri, "Results for a truncated phaseless near field technique," *Electron. Lett.*, vol. 29, no. 5, pp. 505–506, 1993.
[17] G. Lenoe, R. Pierri, and F. Soldovieri, "On the performance of two algorithms in phaseless antenna measurements," in *Proc. 10th Int. Conf. Antennas Propag.*, Apr. 1997, pp. 136–141.
[18] H. Fan, "Far field radiated emission prediction from magnetic near field magnitude-only measurements of PCBs by genetic algorithm," in *Proc. IEEE Int. Symp. Electromagn. Compat.*, Aug. 2009, pp. 321–324.
[19] H. Fan, "Influence of planar sampling techniques of near field magnitude-only data on predicting far field radiation of PCBs by genetic algorithms," in *Proc. IEEE Int. Symp. Electromagn. Compat.*, Jul. 2010, pp. 501–504.
[20] R. W. Gerchbcrg and W. Saxton, "A practical algorithm for the determination of phase from image and diffraction planar pictures," *Optik*, vol. 35, pp. 237–246, 1972.
[21] A. P. Anderson and S. Stili, "New possibilities for phaseless microwave diagnostics. Part 1: Error reduction techniques," *IEE Proc. H Microwaves, Antennas Propag.*, vol. 132, pp. 291–298, 1985.
[22] J. A. Lord, G. G. Cook, and A. P. Anderson, "Reconstruction of the excitation of array antennas from the measured near-field intensity using phase retrieval," *IEE Proc. H Microwaves, Antennas Propag.*, vol. 139, pp. 392–396, Aug. 1992.
[23] J. A. Lord, G. G. Cook, and A. P. Anderson, "Retrieval of the driving current of a dipole array from the radiated field magnitude, " in *Proc. Euro. Microwave Conf.*, 1991, pp. 623–628.
[24] P. Wilson, "On correlating TEM cell and OATS emission measurements," *IEEE Trans. Electromagn. Compat.*, vol. 37, no. 1, pp. 1–16, Feb. 1995.
[25] J. R. Regue, M. Ribo, J. Gomila, A. Perez, and A. Martin, "Modeling of radiating equipment by distributed dipoles using metaheuristics methods," in *Proc. Int. Symp. Electromagn. Compat.*, 2005, pp. 596–601.
[26] C. A. Balanis, Antenna Theory Analysis and Design. Hoboken, NJ, USA: Wiley, 2005.
[27] T. B. Hansen and A. D. Yagbjian, *Plane-Wave Theory of Time-Domain Fields*, D. G. Dudley, Ed. Piscataway, NJ, USA: IEEE Press, 1999.
[28] Z. Yu *et al.*, "Near-Field H to E transformation using plane wave spectrum theory," in *Proc. IEEE Int. Symp. Electromagn. Compat.*, Aug. 2011, pp. 542–546.
[29] D. Baudry *et al.*, "Plane wave spectrum theory applied to nearfield measurements for electromagnetic compatibility investigations," *IET Sci., Meas. Technol.*, vol. 3, no. 1, pp. 72–83, Jan. 2009.

**Ji Zhang** received the B.S. and M.S. degrees from Tsinghua University, Beijing, China, in 2005 and 2008, respectively, and the Ph.D. degree from the Electromagnetic Compatibility Laboratory, Missouri University of Science and Technology, Rolla, MO, USA, in 2013, all in electrical engineering.

He is currently working for Apple Inc., Cupertino, CA, USA. His research interests include the immunity of integrated circuits to electromagnetic-fields interference, reconstruction of emission sources, power delivery network modeling, and design and optimization for Ethernet series-link and other high-speed interfaces including peripheral component interconnect express, external memory interface, media-independent interface, media-dependent interface, etc.

**Jun Fan** (S'97–M'00–SM'06–F'16) received the B.S. and M.S. degrees from Tsinghua University, Beijing, China, in 1994 and 1997, respectively, and the Ph.D. degree from the University of Missouri-Rolla, Rolla, MO, USA, in 2000, all in electrical engineering.

From 2000 to 2007, he worked for NCR Corporation, San Diego, CA, as a Consultant Engineer. In July 2007, he joined the Missouri University of Science and Technology (formerly University of Missouri-Rolla), and is currently a Professor and the Director of the Missouri S&T EMC Laboratory, Rolla, MO, USA. He also serves as the Director of the National Science Foundation Industry/University Cooperative Research Center for Electromagnetic Compatibility and a Senior Investigator of Missouri S&T Material Research Center. His research interests include signal integrity and electromagnetic interference (EMI) designs in high-speed digital systems, dc power-bus modeling, intrasystem EMI and RF interference, printed circuit board noise reduction, differential signaling, and cable/connector designs.

Dr. Fan served as the Chair of the TC-9 Computational Electromagnetics Committee from 2006 to 2008, the Chair of the Technical Advisory Committee from 2014 to 2016, and a Distinguished Lecturer in 2007 and 2008, in the IEEE Electromagnetic Compatibility (EMC) Society. He currently is an Associate Editor for the IEEE TRANSACTIONS ON ELECTROMAGNETIC COMPATIBILITY and the *IEEE EMC Magazine*. He received an IEEE EMC Society Technical Achievement Award in August 2009.